ADVANCED MATERIALS

Supporting Information

for *Adv. Mater.*, DOI: 10.1002/adma.202001136

Reconstruction-Determined Alkaline Water Electrolysis at Industrial Temperatures

Xiong Liu, Ruiting Guo, Kun Ni, Fanjie Xia, Chaojiang Niu, Bo Wen, Jiashen Meng, Peijie Wu, Jinsong Wu,* Xiaojun Wu, and Liqiang Mai**

Supporting Information

Reconstruction-Determined Alkaline Water Electrolysis at Industrial Temperatures

Xiong Liu, Ruiting Guo, Kun Ni, Fanjie Xia, Chaojiang Niu, Bo Wen, Jiashen Meng, Peijie Wu, Jinsong Wu,* Xiaojun Wu, and Liqiang Mai**

X. Liu, R. Guo, F. Xia, Dr. C. Niu, B. Wen, J. Meng, P. Wu, Prof. J. Wu, Prof. L. Mai, State Key Laboratory of Advanced Technology for Materials Synthesis and Processing, Wuhan University of Technology, Wuhan 430070, China

Prof. L. Mai, Foshan Xianhu Laboratory of the Advanced Energy Science and Technology Guangdong Laboratory, Xianhu hydrogen Valley, Foshan 528200, China

Dr. K. Ni, Prof. X. Wu, Hefei National Laboratory for Physical Sciences at the Microscale, School of Chemistry and Materials Sciences, CAS Key Laboratory of Materials for Energy Conversion, CAS Center for Excellence in Nanoscience, iChEM (Collaborative Innovation Center of Chemistry for Energy Materials), University of Science and Technology of China, Hefei, Anhui 230026, China

E-mail: mlq518@whut.edu.cn; wujs@whut.edu.cn; nikun@ustc.edu.cn

Experimental section

1.1 Synthesis of $NiMoO_4$ nanowire array ($NiMoO_4$/NF) catalyst.

$NiMoO_4$ was derived from $NiMoO_4 \cdot xH_2O$ via calcination at 550 ℃ in air for 2 h, and the synthesis of $NiMoO_4 \cdot xH_2O$ referred to the previous works.[1,2] In detail, $Ni(NO_3)_2 \cdot 6H_2O$ (30 mmol) and $Na_2MoO_4 \cdot 2H_2O$ (30 mmol) were dissolved into deionized water (360 mL), respectively. The formed transparent solution was then transferred into Teflon-lined autoclave (500 mL) and four pieces of nickel foam were added. The nickel foam sample was taken out after reaction at 120 ℃ for 6 h, and then washed and vacuum drying. The $NiMoO_4 \cdot xH_2O$ precursor was obtained. Finally, after calcination at 550 ℃ in air for 2 h, the $NiMoO_4$ arrays were obtained for subsequent electrocatalytic testing.

1.2 Synthesis of MoO_2-Ni heterostructured nanowire array catalyst.

MoO_2-Ni catalyst was derived from $NiMoO_4 \cdot xH_2O$ via phase-separation treatment in the reducing atmosphere, which referred to our previous work.[1]

1.3 Synthesis of NiFe layered double hydroxide (LDH) nanosheet array (NiFe-LDH/NF) catalyst.

The synthesis of NiFe-LDH/NF referred to the reported method.[3]

1.4 Synthesis of $CoMoO_4$ nanosheet array ($CoMoO_4$/NF) catalyst.

$Co(NO_3)_2 \cdot 6H_2O$ (2 mmol) and $Na_2MoO_4 \cdot 2H_2O$ (2 mmol) were dissolved into deionized water (60 mL) to form the homogeneous transparent solution. The solution was then transferred into Teflon-lined autoclave (100 mL) and one piece of nickel foam (3 cm * 4 cm) was vertically placed in the reactor. After reaction at 120 ℃ for 6 h and washed, the Co-Mo-O precursor was obtained. Finally, the $CoMoO_4$/NF was obtained after calcination at 550 ℃ in air for 2 h.

1.5 Characterizations.

Scanning electron microscopy (SEM) images were obtained by a JEOL JSM-7100F scanning electron microscope. Transmission electron microscopy (TEM), high-resolution TEM (HRTEM), high-angle annular dark-field scanning transmission electron microscopy (HAADF-STEM) images, the selected area electron diffraction (SAED) patterns, and energy-dispersive X-ray spectroscopy (EDX) elemental mappings were collected by a 300 kV double corrected Titan G260-300 electron microscope. Electron tomography was carried out by a Talos F200S. X-ray photoelectron spectroscopy (XPS) measurements were performed on an ESCALAB 250 Xi spectrometer with an Al Ka X-ray radiation for excitation. In situ low-/high-temperature Raman measurements were recorded using a combined system of HORIBA HR EVO Raman system (633 nm laser) and an electrochemical workstation (CHI 760E). The heating temperature was controlled by silicone rubber heating plate, and the solution temperature was measured by a digital display thermometer.

1.6 Electrochemical measurements.

Catalytic measurements were carried out by a CHI 760E electrochemical workstation (Chenhua, China). For the alkaline OER or HER measurements, a standard three-electrode system was applied. Fresh 1 M KOH served as testing solution. The nickel foam samples were directly served as a working electrode, and an unused Hg/HgO electrode and a graphite rod were used as a reference electrode and a counter electrode, respectively. After each test in a high temperature solution, the new Hg/HgO electrode was used for the next test due to its limited service life. For AWE measurements, two-

electrode system was applied. The cat.-51.9 and MoO_2-Ni arrays were used as an anode and a cathode, respectively. Linear sweep voltammetry (LSV) curves were recorded at a slow scan rate of 1 mV s^{-1}, and the data were dealt with iR compensation. Chronopotentiometric measurements were carried out at 10 mA cm^{-2} in fresh 1 M KOH with controllable solution temperature controlled by heating equipment.

1.7 Calculation method.

All the density function theory (DFT) calculations were done by using Vienna ab-initio simulation package (VASP) software.[4] The exchange correlation energy was described by generalized gradient approximation (GGA)[5] method with Perdew-Burke-Ernzerhof (PBE) function[6]. The projector-augmented wave (PAW) method was used with 400 eV basis set cut off. Electronic calculations were spin unrestricted. Gaussian type smearing was adopted with sigma value of 0.2 eV. Grimme method of DFT-D3 long-term force correction was applied. The strong coulomb repulsion of electrons in transition metals was considered with GGA+U method, with applying 6.6 eV of U-J value on Ni element.[7] The self-consistent field (SCF) energy tolerance was 0.01 meV and the force tolerance of geometry optimization was 0.02 eV/Å. In order to get correct magnetic ground state, a starting magnetic moment of 2 μ_B for Ni, 0 μ_B for O and H was set and the charge mixing related parameters were carefully tested for each structure. The surface models and the boundary models were firstly optimized with 1×1×1 K point set, then single energy calculations were done with 2×2×1 K point set. The COHP calculation was done by reading wave functions calculated by VASP by local-orbital basis suite towards electronic-structure reconstruction (LOBSTER) software.[8]

The models were primarily built by using Materials Studio software. The bulk NiOOH phase was adopted from our previous report on orthorhombic-NiOOH.[9] The NiOOH (011) surface model was built by cleaving surface from orthorhombic-NiOOH model with the thickness of 3 layers (7.17Å) and making a 2×2 supercell with ~13 Å vacuum space. The O or OH vacancies were achieved by directly removing the corresponding atoms in the model and followed by full geometry optimizations. The NiOOH (011)-NiOOH (011) twin boundary model used in our simulation was a twin boundary. The building procedure could be described as following: I. Cleaved and built two distinct surface model with direction (011) and $(0\bar{1}1)$ based on the fully optimized bulk crystal model of NiOOH. The angle

between (011) surface and the $(0\bar{1}1)$ surface was 68.77° (Figure S13a). In contrast, the TEM observation of NiOOH (011)-NiOOH (011) boundary angle of ~63° was shown in Figure S13b. The cleaved surface models were shown in Figure S13c,d. II. Built vacuum slab for each surface model. III. Built boundary by moving two layers into a suitable distance, which meant the newly formed Ni-O bonds had a similar length with those in bulk phase (Figure S13e). IV. Rebuilt the lattice length along the surface direction to delete the vacuum area that previously built in step II and created a vacuum space in the direction out of paper to hold species in OER reactions. Then the boundary model was fully relaxed (Figure S13f). We could find that the basic Ni-O framework did not go through a remarkable change during optimization, but only a slight distortion in boundary was observed, showing that our twin boundary model had a good rationality. The optimized boundary model had a twin angle of ~66°, which was close to the TEM observation of ~63°. The difference of ~3° could be originated from the errors both from simulation methods and experimental results. We should note that the NiOOH $(0\bar{1}1)$-NiOOH (011) boundary model was actually equivalent to a NiOOH (011)-NiOOH (011) twin boundary model, thus the NiOOH (011)-NiOOH (011) twin boundary model was denoted in our manuscript.

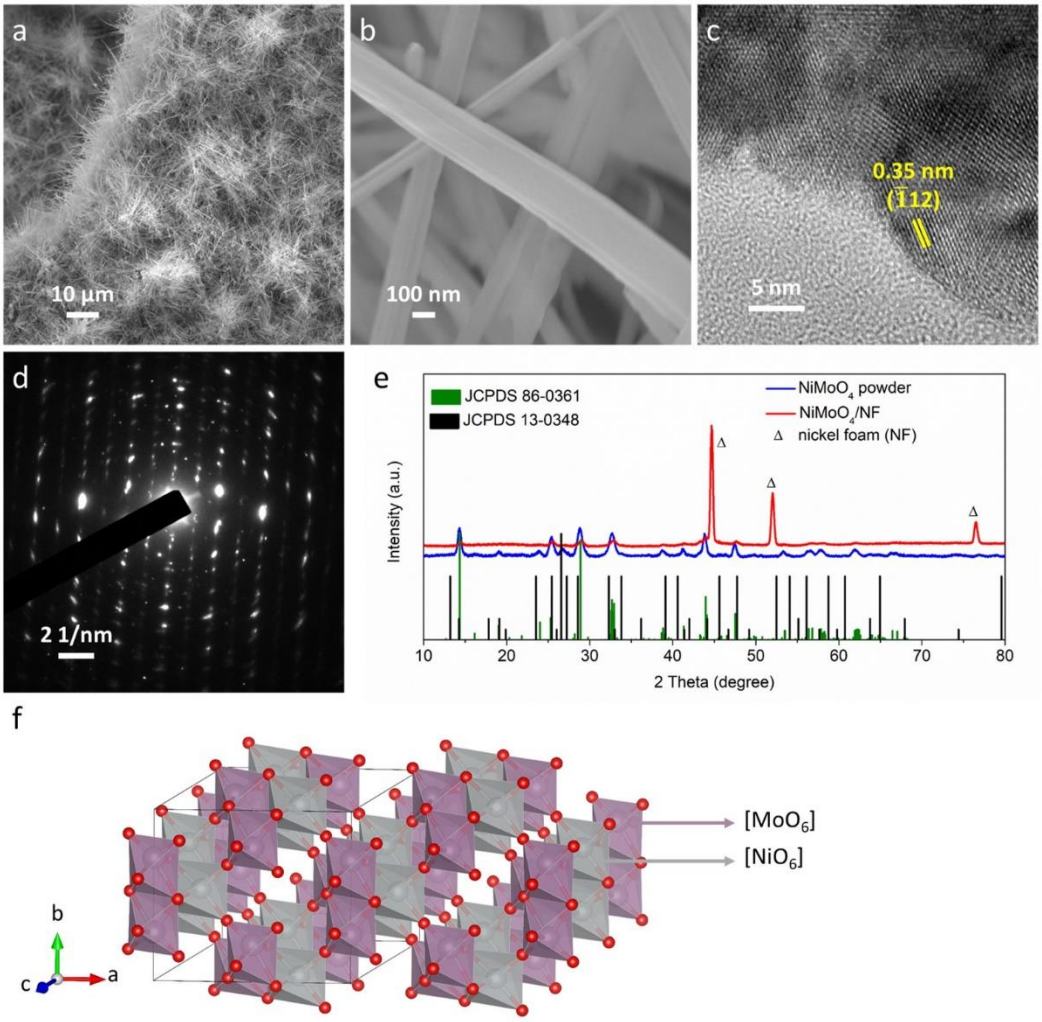

Figure S1. a,b) SEM images of $NiMoO_4$/NF. c) HRTEM image and d) SAED pattern of $NiMoO_4$. e) XRD patterns of $NiMoO_4$/NF and $NiMoO_4$ powder. f) Crystal structure of $NiMoO_4$ (JCPDS No. 86-0361).

Due to the strong XRD peaks of nickel foam substrate, the intensity of peaks for $NiMoO_4$ phase is very weak. Therefore, the $NiMoO_4$ powder was prepared using the same synthesis method. As shown in Figure S1e, some visible peaks for $NiMoO_4$/NF can also be found in the XRD pattern for $NiMoO_4$ powder. Further analyses show that the peaks are well assigned to $NiMoO_4$ phase (JCPDS No. 86-0361; JCPDS No. 13-0348).

The crystal structure for $NiMoO_4$ (JCPDS No. 86-0361) is shown in Figure S1f. It shows the monoclinic system with the space group of C2/m, and contains the NiO_6 or MoO_6 octahedron.

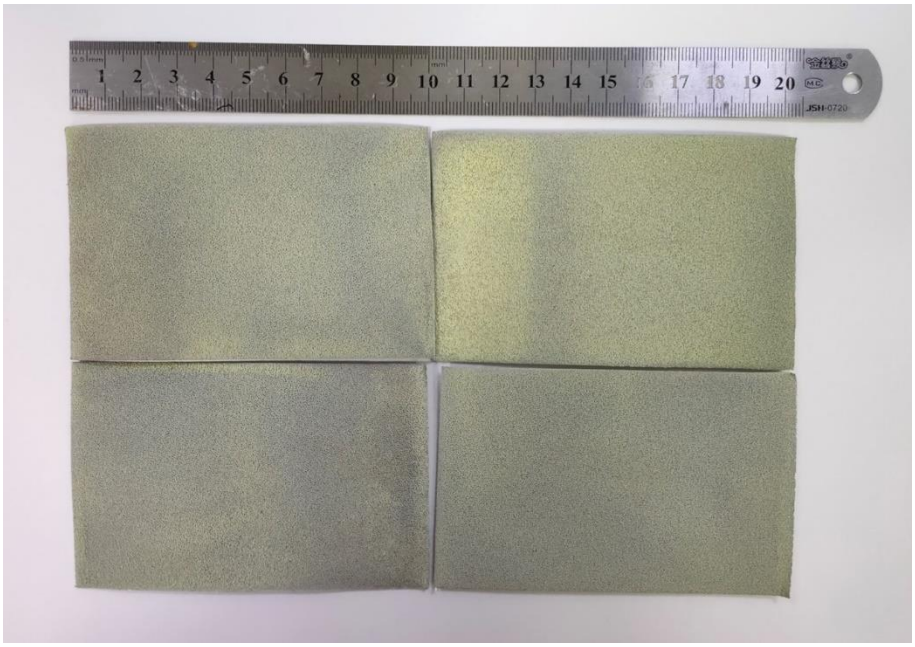

Figure S2. Optical photo of four pieces of $NiMoO_4$/NF after one-pot hydrothermal synthesis and subsequent calcination.

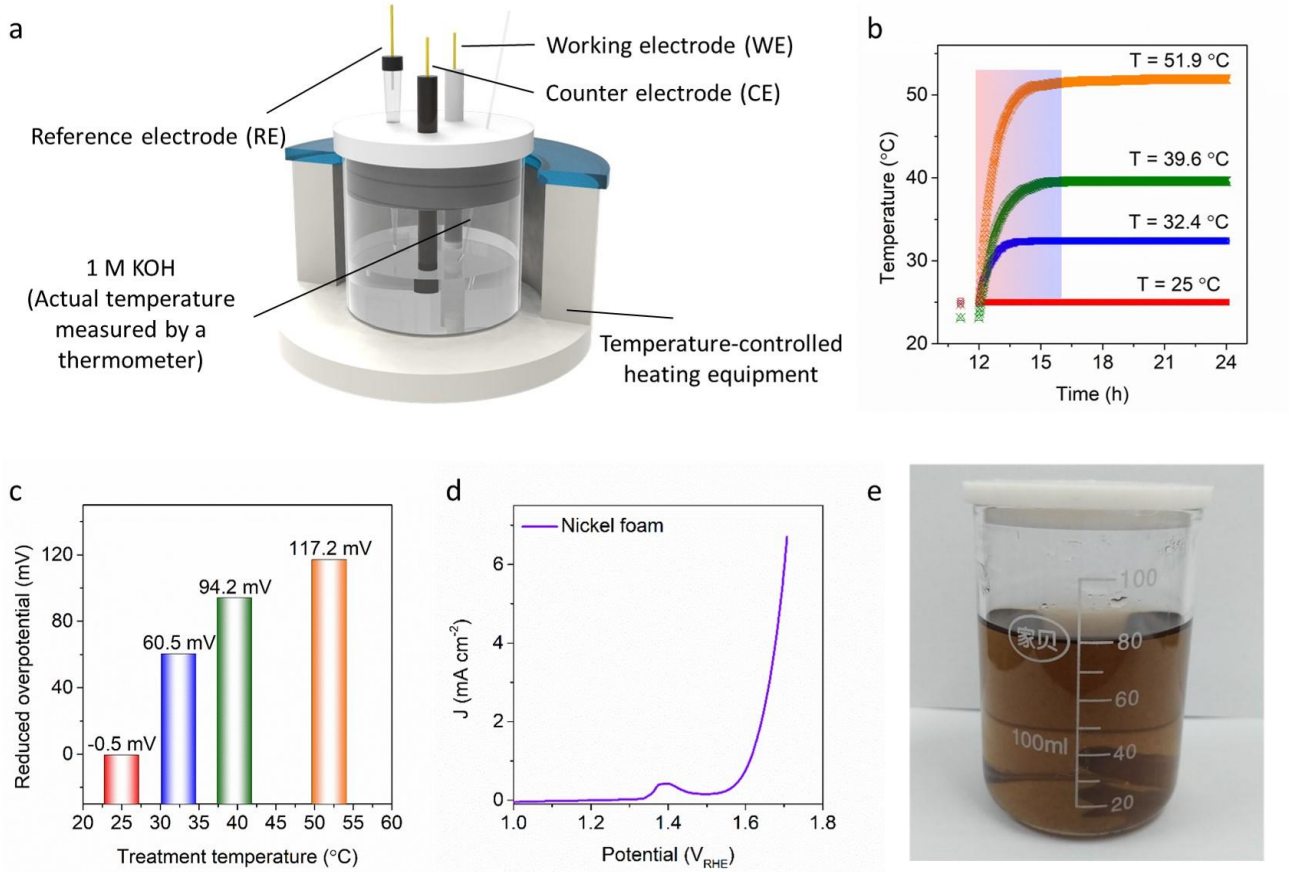

Figure S3. a) Schematic diagram of temperature-controlled three-electrode device. b) Corresponding solution temperature for cat.-T in Figure 1a, indicating the solution temperatures can be raised from

room temperature to the corresponding temperature (T) within 3 h. c) Temperature-dependent potential differences of ΔV. d) LSV curve of blank nickel foam tested at 1 mV s^{-1} and 25.0 ℃. e) Optical photo of KOH solution after OER at 51.9 ℃ using carbon cloth substrate as a working electrode. The solution takes on a brown color due to the electro-oxidation and stripping of carbon into the solution.

The electro-oxidation induced exfoliation phenomenon suggests that the carbon-based substrates are not suitable for OER, especially for harsh testing conditions. Ren et al. reported a water electrolytic oxidation method for the synthesis of clean graphene oxide sheets based on commercial flexible graphite paper.[10] Differently, the operation was carried out in acid solution. During the electro-oxidation in H_2SO_4, the graphite paper transformed into graphite intercalation compound paper due to its electrochemical intercalation. The sample was then oxidized to yellow-colored graphite oxide along with severe swelling and exfoliation. Finally, the exfoliated graphite oxide sheets were obtained via sonication.

Similar to the reported work, the electro-oxidation and exfoliation processes also happen on carbon cloth substrate in alkali in our work. Especially, the OER catalytic kinetic of catalysts is enhanced under the high-temperature condition. This promotes faster generation and diffusion of O_2 gas and thus accelerates the stripping of carbon electrode.

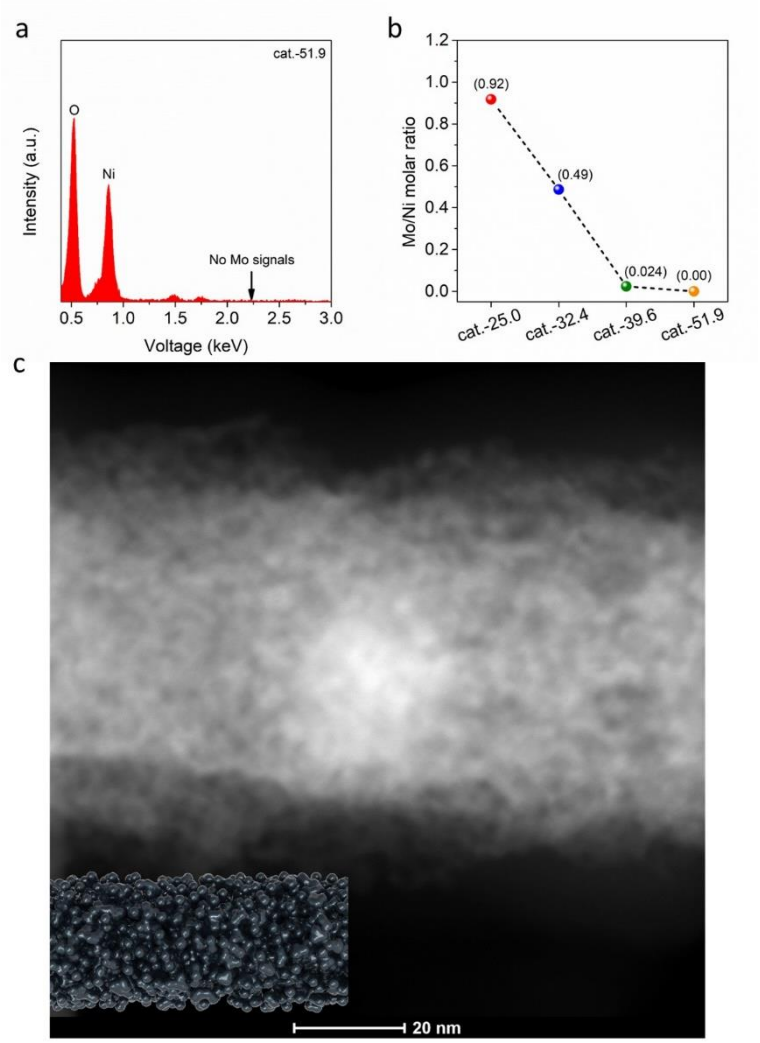

Figure S4. a) EDX spectrum of cat.-51.9, suggesting the absence of Mo element. b) EDX results of Mo/Ni molar ratios of cat.-T (T = 25.0, 32.4, 39.6, 51.9). c) HAADF STEM image of cat.-51.9 with the corresponding schematic diagram (inset).

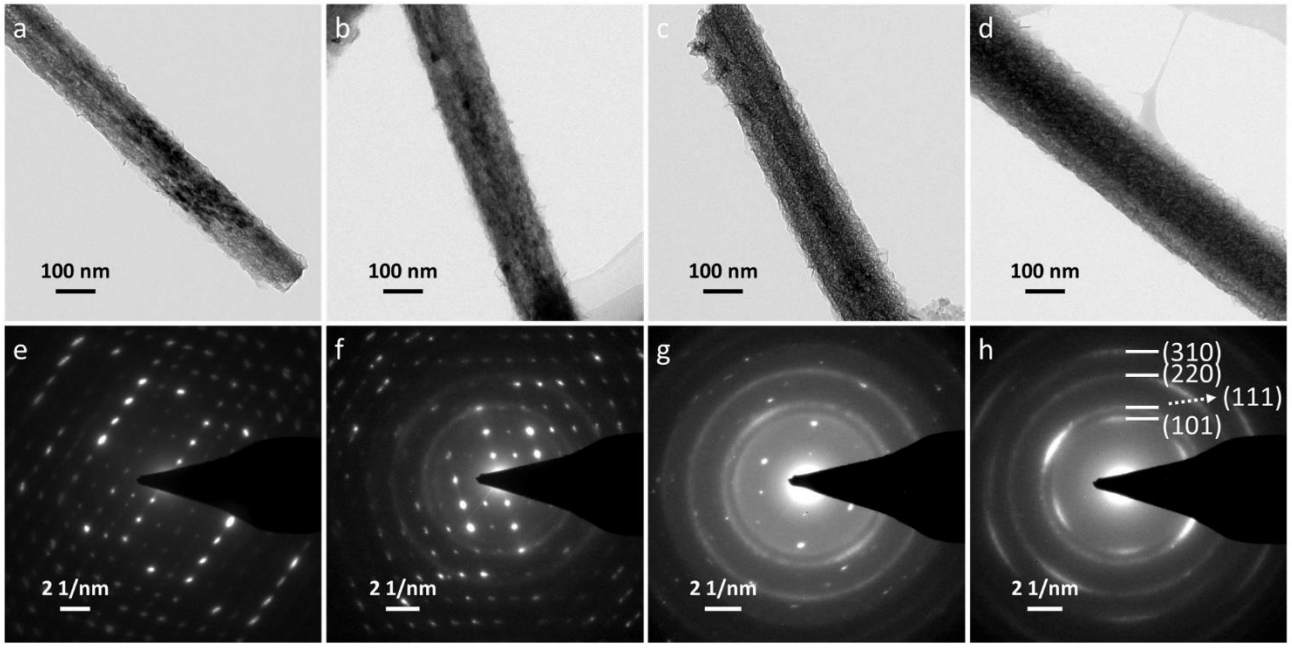

Figure S5. a-d) TEM images and e-h) SAED patterns of cat.-T (T = 25.0, 32.4, 39.6, 51.9).

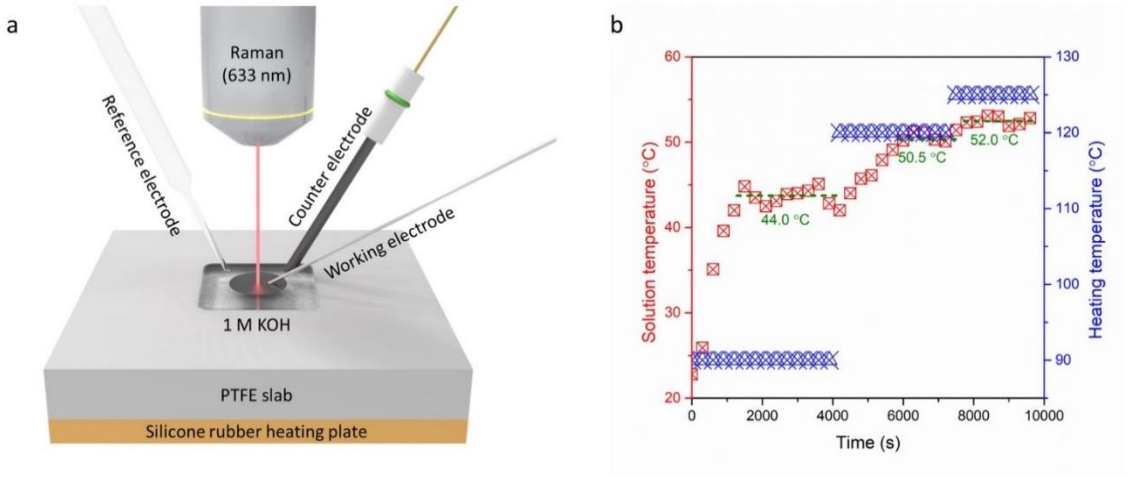

Figure S6. a) Schematic illustration of temperature-controllable Raman-electrochemistry coupling system for in situ Raman measurements. b) Relationship between the heating temperature and real temperature of solution.

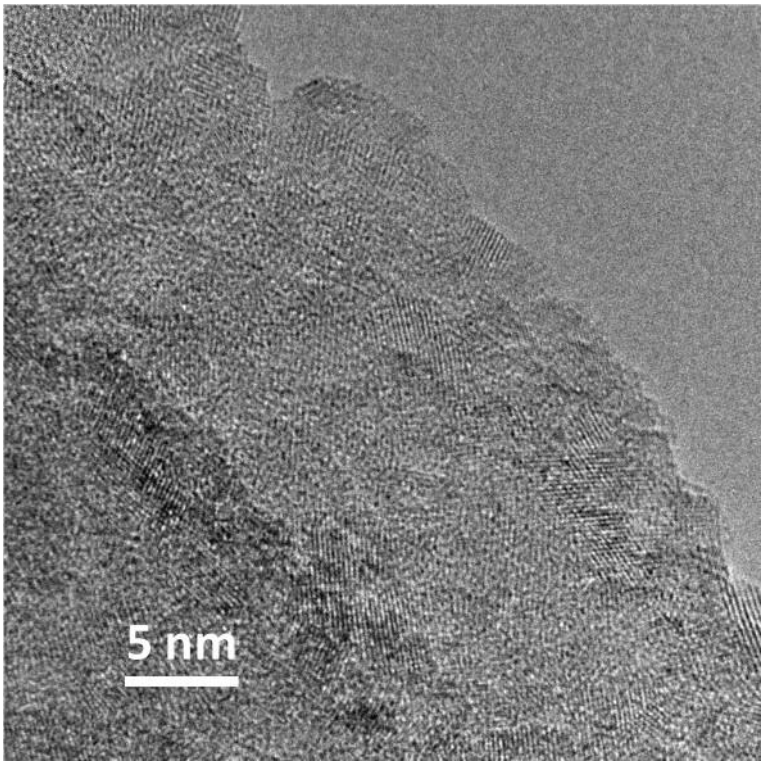

Figure S7. HRTEM image for the outermost layer of cat.-39.6 nanowire.

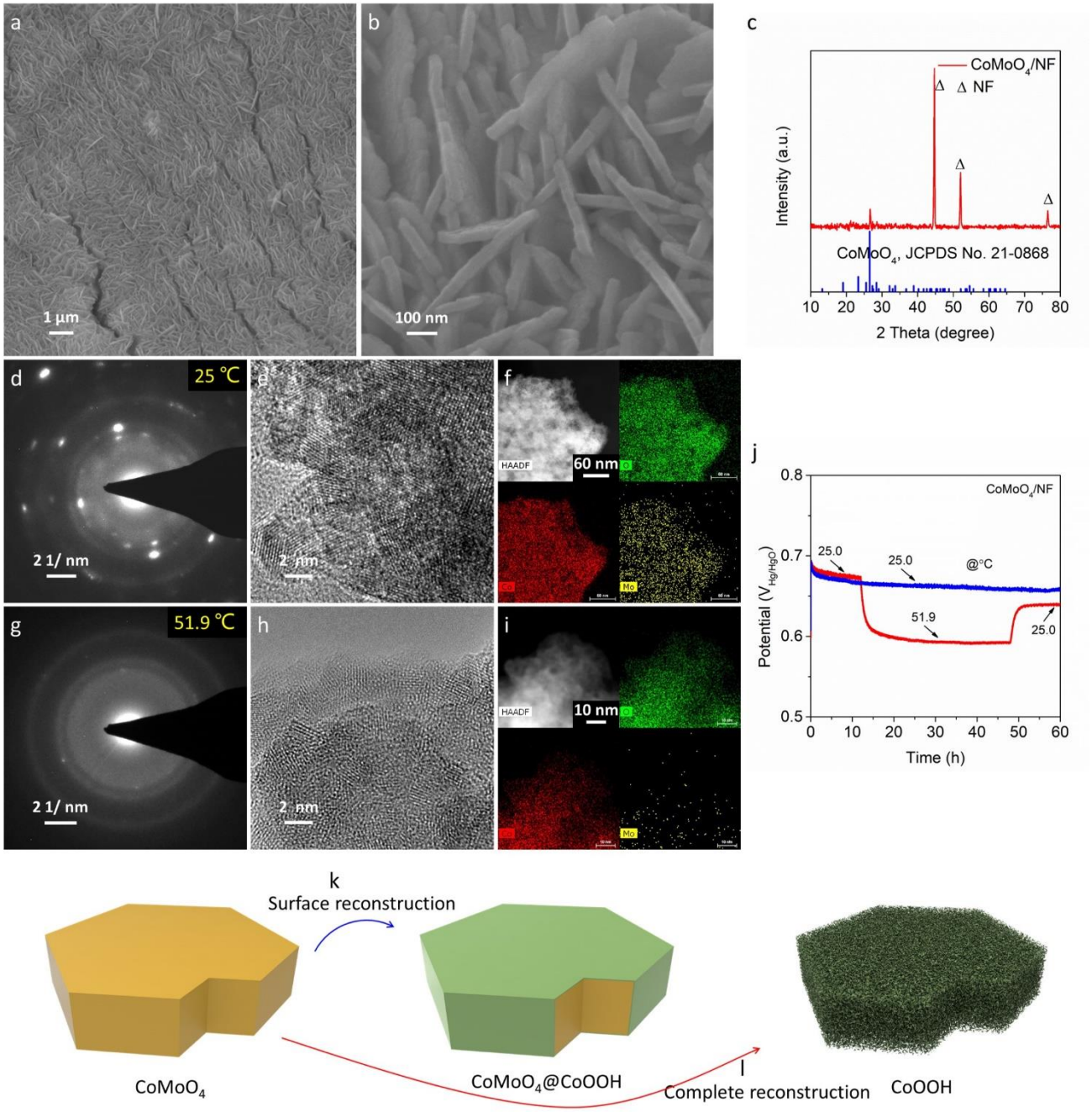

Figure S8. a,b) SEM images of Co-Mo-O precursor. c) XRD pattern of $CoMoO_4$ nanosheet arrays grown on the nickel foam ($CoMoO_4$/NF). d) SAED pattern, e) HRTEM, and f) HAADF STEM images and the corresponding mappings of $CoMoO_4$ pre-catalyst after OER at 25.0 ℃. g) SAED pattern, h) HRTEM, and i) HAADF STEM images and the corresponding mappings of $CoMoO_4$ pre-catalyst after OER at 51.9 ℃. j) Chronopotentiometric measurements of $CoMoO_4$/NF under low-/high-temperature conditions. Schematic diagram for the formation of (k) $CoMoO_4$@CoOOH via surface reconstruction at 25.0 ℃ and (l) CoOOH via complete reconstruction at 51.9 ℃ based on $CoMoO_4$ pre-catalyst.

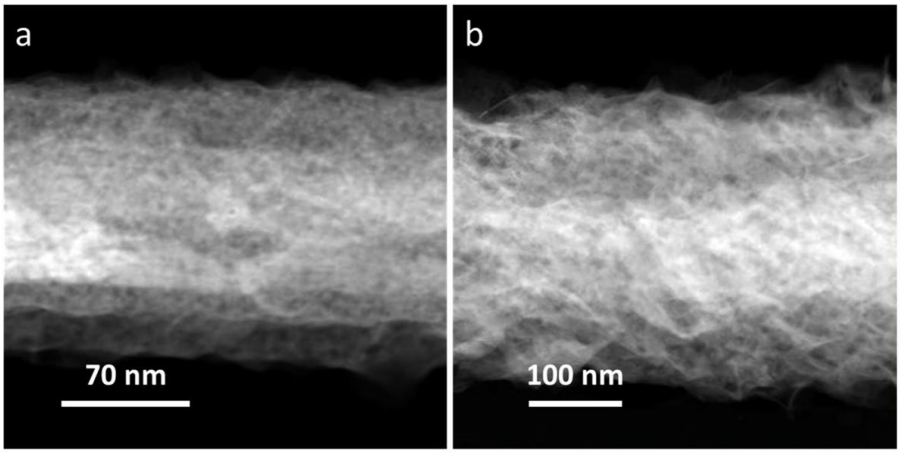

Figure S9. a,b) HAADF STEM images of $NiMoO_4$ pre-catalyst after (a) in situ and (b) ex situ reconstruction.

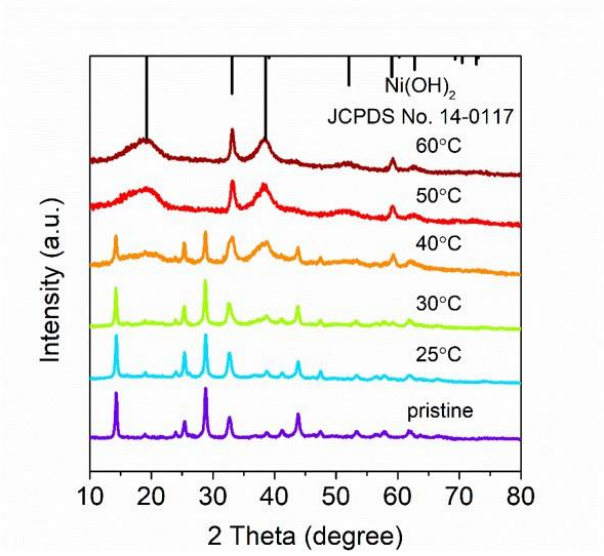

Figure S10. XRD patterns of $NiMoO_4$ powder and products after soaking in 1 M KOH at different temperatures (25, 30, 40, 50, 60 ℃).

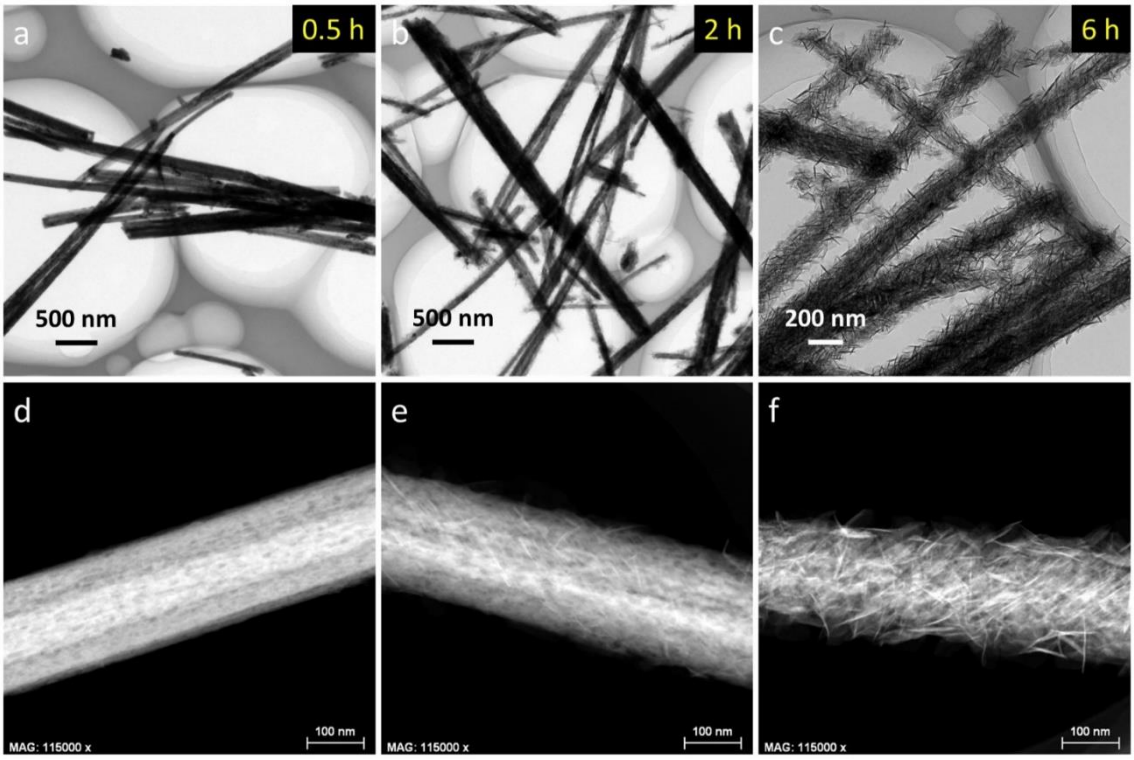

Figure S11. a-c) TEM images of $NiMoO_4$-derived nanowires after soaking in 1 M KOH at 51.9 °C for (a) 0.5, (b) 2, and (c) 6 h. d-f) The corresponding HAADF STEM images.

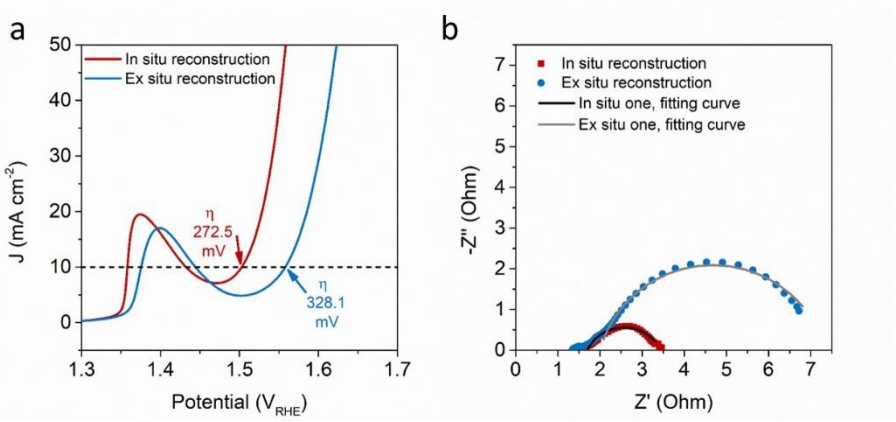

Figure S12. a) LSV curves and b) electrochemical impedance spectroscopy (EIS) results at 0.65 $V_{Hg/HgO}$ with the fitting curves of $NiMoO_4$ pre-catalyst after in/ex situ reconstruction.

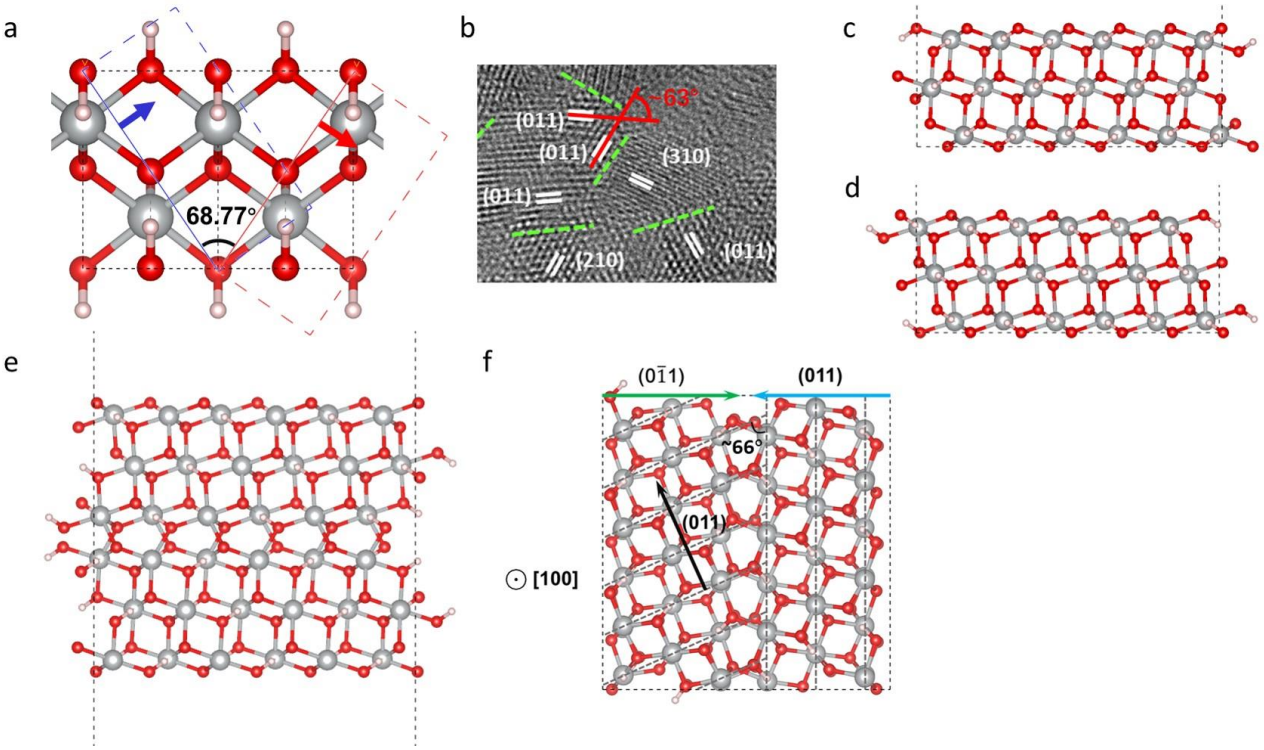

Figure S13. a) (011) and (0$\bar{1}$1) surface directions in bulk NiOOH crystal. Blue arrow indicates (0$\bar{1}$1) surface and red arrow indicates (011) surface. b) TEM image of the reconstructed NiOOH with a NiOOH (011)-NiOOH (011) twin boundary marked by red line (also see Figure 2d in the manuscript). c) (011) surface with the thickness of three layers. d) (0$\bar{1}$1) surface with the thickness of three layers. e) The NiOOH (011)-NiOOH (011) twin boundary model. f) The optimized NiOOH (011)-NiOOH (011) twin boundary model with markings.

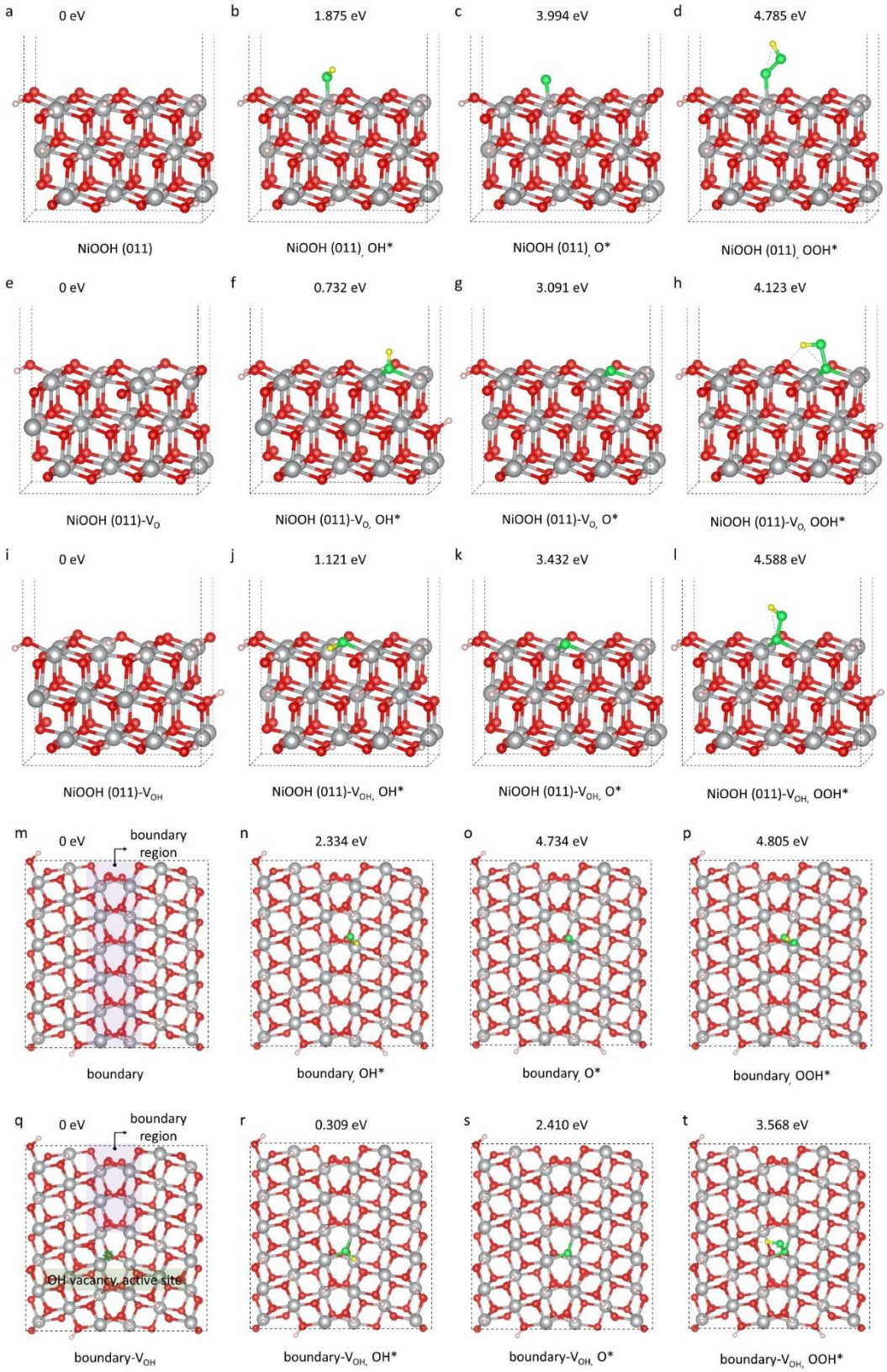

Figure S14. The optimized OER pathways on the different models with the optimal structures at each stage.

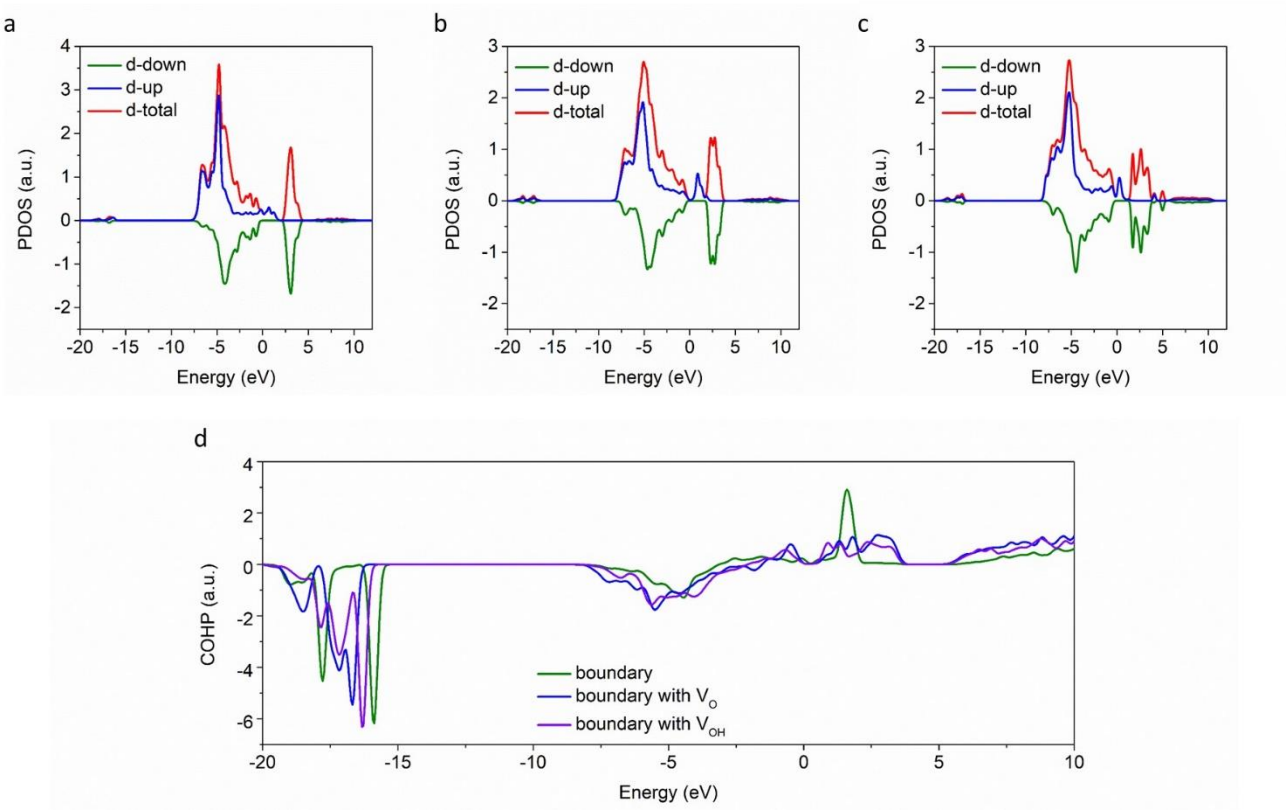

Figure S15. a-c) PDOS of active Ni atom site in (a) NiOOH (011) and (b) boundary models, and Ni-1 atom in (c) boundary with V_O model. (d) COHP between the O* and active Ni atoms.

For boundary with V_O and boundary with V_{OH} models, the COHP between O* and Ni-1 atom and O* and Ni-2 atom is summarized. Comparing the listed Ni PDOS in Figure S15a-c and the Ni-2 PDOS in boundary with V_O model in Figure 4l, the peak of d band at -6.9 eV of Ni-2 atom in boundary with V_O model is obvious and additional. This additional peak is caused by the synergistic effect of O vacancy and grain boundary. When we look at the COHP of the O*-Ni interactions at -6.9 eV, the bonding interaction of O*-Ni in boundary with V_O model is stronger than the bonding interaction in the bounday model without O vacancy. Therefore, we could figure out that the additional d band states at -6.9 eV of Ni cause the stronger Ni-O bonding interaction and enhance the O* adsorption.

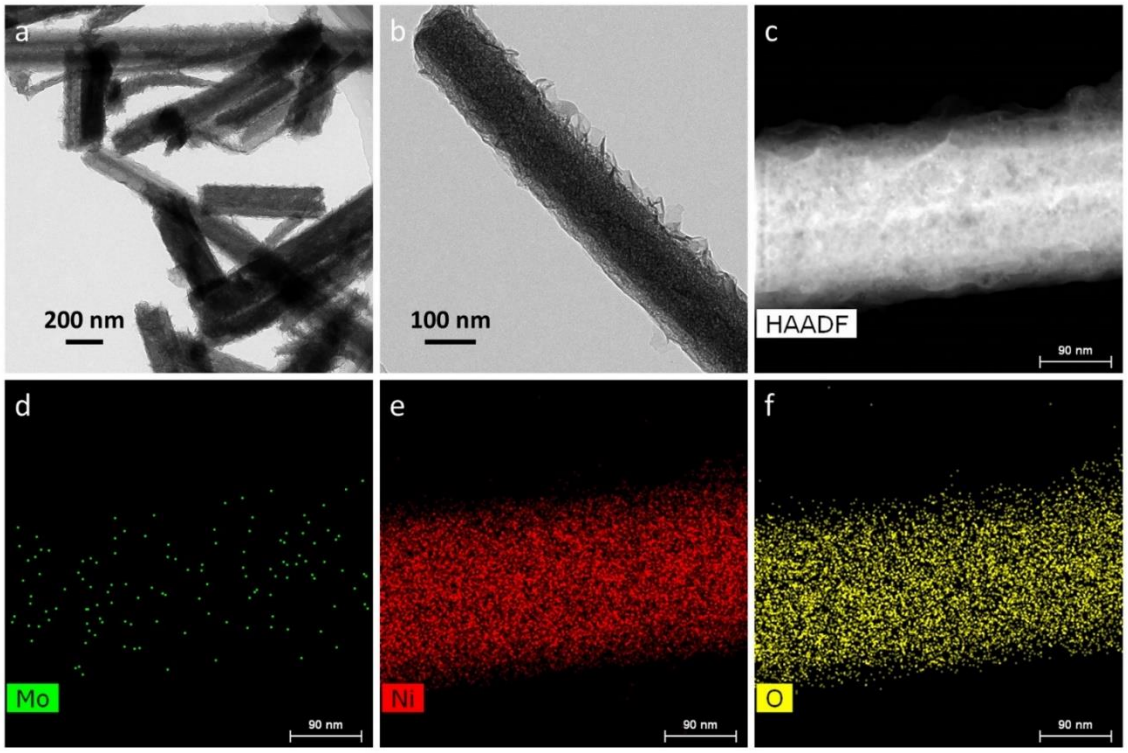

Figure S16. Characterizations on cat.-51.9 after long-term OER testing at 51.9 °C. a,b) TEM and c-f) HAADF STEM images and the corresponding elemental mappings.

These characterizations demonstrate its well-remained nanowire structure and good component stability. The Mo/Ni molar ratio is 0.0013.

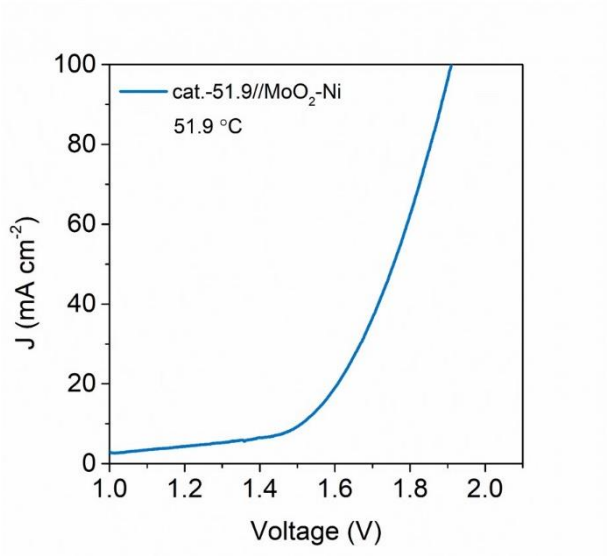

Figure S17. LSV curve of cat.-51.9//MoO_2-Ni array system for AWE tested at 1 mV s^{-1} in 1 M KOH at 51.9 °C.

Table S1. Comparisons of alkaline OER activity and stability between cat.-51.9 and other recently reported non-noble-metal catalysts.

Catalysts	Electrolytes	Catalytic activity	Durability (h)	Testing temperatures (℃)	References
cat.-51.9	1 M KOH	274.1, 282.3, 288.0, and 293.2 mV at 15, 20, 25, and 30 mV, respectively	275 h at 10 mA cm^{-2}	25.0	This work
		-	250 h at 10 mA cm^{-2}	51.9	
W-doped $Ni(OH)_2$	1 M KOH	237 mV at 10 mA cm^{-2}	< 3 h in all at various current density	Room temperature	11
Ni_2P-VP_2/NF	1 M KOH	306 mV at 50 mA cm^{-2}	20 h at 10 mA cm^{-2}; 48 h at 50 mA cm^{-2}	Room temperature	12
$Ni_3Fe_{0.5}V_{0.5}$/carbon fiber paper (CFP)	1 M KOH	200 mV at 10 mA cm^{-2}; 264 mV at 100 mA cm^{-2}	60 h at 10 mA cm^{-2}; 60 h at 100 mA cm^{-2}	25.0	13
$La_{0.5}Sr_{1.5}Ni_{0.7}Fe_{0.3}O_{4.04}$	O_2-saturated 1 M KOH	360 mV at 10 mA cm^{-2}	24 h at 10 A g^{-1}	Room temperature	14
Ni/C-600/NF	1 M KOH bubbled with oxygen	265 mV at 10 mA cm^{-2}	-	Room temperature	15
CeO_x/$NiFeO_x$	Purified 1 M KOH with O_2 bubbling	-	96 h at 20 mA cm^{-2}	25.0	16
$Ni_{11}(HPO_3)_8(OH)_6$/NF	1 M KOH	232 mV at 10 mA cm^{-2}	25 h at overpotential of 240 mV	Room temperature	17
p-$Cu_{1-x}NNi_{3-y}$/FeNiCu	1 M KOH	280 mV at 10 mA cm^{-2}	24 h at 10 mA cm^{-2}	Room temperature	18
S|NiN_x species embedded in porous carbon/exfoliated graphene (EG)	1 M KOH	280 mV at 10 mA cm^{-2}	<10 h at 10 mA cm^{-2}	Not mentioned	19
Fe-Ni@NC-CNT	N_2-saturated 1 M KOH	274 mV at 10 mA cm^{-2}	<12 h at 10 mA cm^{-2}	Room temperature	20
Ni-MnO/rGO aerogel	O_2-saturated 0.1 M KOH	370 mV at 10 mA cm^{-2}	<3 h at 10 mA cm^{-2}	Not mentioned	21
$Zn_{0.2}Co_{0.8}OOH$	1 M KOH	235 mV at 10 mA cm^{-2}	40 h at 20 mA cm^{-2}	Not mentioned	22
Hierarchical Ni-Co-P	1 M KOH bubbled with oxygen before OER	270 mV at 10 mA cm^{-2}	20 h (chronoamperometry measurement)	Room temperature	23
Cr-doped FeNi–P nanoparticles encapsulated into N-doped carbon nanotubes	1 M KOH	240 mV at 10 mA cm^{-2}	20 h at 10 mA cm^{-2}	25.0	24
NiFe/laser-induced graphere (LIG)	0.1 M KOH	240-279 mV at 10 mA cm^{-2}	<5 h at 10 mA cm^{-2}	Not mentioned	25
$LaFe_xNi_{1-x}O_3$	O_2-saturated 1 M KOH	302 mV at 10 mA cm^{-2}	20 h at 1.53 V_{RHE}	Not mentioned	26
Tannin-NiFe/CFP	1 M KOH	290 mV at 10 mA cm^{-2}	24 h at 10 mA cm^{-2}	Not mentioned	27
La_2NiMnO_6 nanoparticles	1 M KOH purged with oxygen for 30 min	~370 mV at 10 mA cm^{-2}	<14 h (chronoamperometry measurement)	Not mentioned	28
NiFe LDH on carbon cloth	1 M KOH	-	20 h at 500 mA cm^{-2}	80.0	29

Table S2. COHP integration values from -22 eV to Fermi level (0 eV) between adsorbate O* and the corresponding bonded Ni atoms.

Models	Interaction	Integral value for spin up	Integral value for spin down	Up+down	Total strength of Ni-O interaction
Boundary	No.1:O172-Ni86	-2.9753	-3.33106	-6.30636	-6.3064
Boundary with V_O	No.1:O147-Ni70	-2.40082	-2.53658	-4.9374	-9.7414
	No.2:O147-Ni80	-2.31089	-2.49306	-4.80395	
Boundary with V_{OH}	No.1:O164-Ni79	-2.31034	-2.61668	-4.92702	-9.6059
	No.2:O164-Ni85	-2.21089	-2.46795	-4.67884	

References

[1] X. Liu, K. Ni, C. J. Niu, R. T. Guo, W. Xi, Z. Y. Wang, J. S. Meng, J. T. Li, Y. W. Zhu, P. J. Wu, Q. Li, J. Luo, X. J. Wu, L. Q. Mai, *ACS Catal.* **2019**, *9*, 2275.

[2] S. J. Peng, L. L. Li, H. B. Wu, S. Madhavi, X. W. Lou, *Adv. Energy Mater.* **2014**, *5*, 1401172.

[3] Z. H. Li, M. F. Shao, H. L. An, Z. X. Wang, S. M. Xu, M. Wei, D. G. Evans, X. Duan, *Chem. Sci.* **2015**, 6, 6624.

[4] J. Hafner, *J. Comput. Chem.* **2008**, *29*, 2044.

[5] J. P. Perdew, K. Burke, M. Ernzerhof, *Phys. Rev. Lett.* **1996**, *77*, 3865.

[6] M. Ernzerhof, G. E. Scuseria, *J. Chem. Phys.* **1999**, *110*, 5029.

[7] D. Friebel, M. W. Louie, M. Bajdich, K. E. Sanwald, Y. Cai, A. M. Wise, M. -J. Cheng, D. Sokaras, T. -C. Weng, R. Alonso-Mori, R. C. Davis, J. R. Bargar, J. K. Nørskov, A. Nilsson, A. T. Bell, *J. Am. Chem. Soc.* **2015**, *137*, 1305.

[8] S. Maintz, V. L. Deringer, A. L. Tchougreeff, R. Dronskowski, *J. Comput. Chem.* **2016**, *37*, 1030.

[9] X. Liu, K. Ni, B. Wen, R. T. Guo, C. J. Niu, J. S. Meng, Q. Li, P. J. Wu, Y. W. Zhu, X. J. Wu, L. Q. Mai, *ACS Energy Lett.* **2019**, *4*, 2585.

[10] S. F. Pei, Q. W. Wei, K. Huang, H. -M. Cheng, W. C. Ren, *Nat. Commun.* **2018**, *9*, 145.

[11] J. Q. Yan, L. Q. Kong, Y. J. Ji, J. White, Y. Y. Li, J. Zhang, P. F. An, S. Z. Liu, S. -T, Lee, T. Y. Ma, *Nat. Commun.* **2019**, *10*, 2149.

[12] H. J. Yan, Y. Xie, A. P. Wu, Z. C. Cai, L. Wang, C. G. Tian, X. M. Zhang, H. G. Fu, *Adv. Mater.* **2019**, *31*, 1901174.

[13] J. Jiang, F. F. Sun, S. Zhou, W. Hu, H. Zhang, J. C. Dong, Z. Jiang, J. J. Zhao, J. F. Li, W. S. Yan, M. Wang, *Nat. Commun.* **2018**, *9*, 2885.

[14] R. P. Forslund, W. G. Hardin, X. Rong, A. M. Abakumov, D. Filimonov, C. T. Alexander, J. T. Mefford, H. Lyer, A. M. Kolpak, K. P. Johnston, K. J. Stevenson, *Nat. Commun.* **2018**, *9*, 3150.

[15] H. Sun, Y. B. Lian, C. Yang, L. K. Xiong, P. W. Qi, Q. Q. Mu, X. H. Zhao, J. Guo, Z. Deng, Y. Peng, *Energy Environ. Sci.* **2018**, *11*, 2363.

[16] K. Obata, K. Takanabe, *Angew. Chem. Int. Ed.* **2018**, *57*, 1616.

[17] P. W. Menezes, C. Panda, S. Loos, F. Bunschei-Bruns, C. Walter, M. Schwarze, X. H. Deng, H. Dau, M. Driess, *Energy Environ. Sci.* **2018**, *11*, 1287.

[18] Y. P. Zhu, G. Chen, Y. J. Zhong, Y. B. Chen, N. N. Ma, W. Zhou, Z. P. Shao, *Nat. Commun.* **2018**, *9*, 2326.

[19] Y. Hou, M. Qiu, M. G. Kim, P. Liu, G. Nam, T. Zhang, X. D. Zhuang, B. Yang, J. Cho, M. W. Chen, C. Yuan, L. C. Lei, X. L. Feng, *Nat. Commun.* **2019**, *10*, 1392.

[20] X. J. Zhao, P. Pachfule, S. Li, J. R. J. Simke, J. Schmidt, A. Thomas, *Angew. Chem. Int. Ed.* **2018**, *57*, 8921.

[21] G. T. Fu, X. X. Yan, Y. F. Chen, L. Xu, D. M. Sun, J. -M, Lee, Y. W. Tang, *Adv. Mater.* **2018**, *30*, 1704609.

[22] Z. -F. Huang, J. J. Song, Y. H. Du, S. B. Xi, S. Dou, J. M. V. Nsanzimana, C. Wang, Z. C. J. Xu, X. Wang, *Nat. Energy* **2019**, *4*, 329.

[23] E. L. Hu, Y. F. Feng, J. W. Nai, D. Zhao, Y. Hu, X. W. Lou, *Energy Environ. Sci.* **2018**, *11*, 872.

[24] Y. Q. Wu, X. Tao, Y. Qing, H. Xu, F. Yang, S. Luo, C. H. Tian, M. Liu, X. H. Lu, *Adv. Mater.* **2019**, *31*, 1900178.

[25] J. B. Zhang, M. Q. Ren, Y. L. Li, J. M. Tour, *ACS Energy Lett.* **2018**, *3*, 677.

[26] H. P. Wang, J. Wang, Y. C. Pi, Q. Shao, Y. M. Tan, X. Q. Huang, *Angew. Chem. Int. Ed.* **2019**, *58*, 2316.

[27] Y. M. Shi, Y. Yu, Y. Liang, Y. H. Du, B. Zhang, *Angew. Chem. Int. Ed.* **2019**, *58*, 3769.

[28] Y. Tong, J. C. Wu, P. Z. Chen, H. F. Liu, W. S. Chu, C. Z. Wu, Y. Xie, *J. Am. Chem. Soc.* **2018**, *140*, 11165.

[29] R. Chen, S. -F Hung, D. J. Zhou, J. J. Gao, C. J. Yang, H. B. Tao, H. B. Yang, L. P. Zhang, L. L. Zhang, Q. H. Xiong, H. M. Chen, B. Liu, *Adv. Mater.* **2019**, *31*, 1903909.